Early Alzheimer's Disease Detection Using Functional MRI, Modified Census Transform, and Hierarchical Classification

Detección Temprana de la Enfermedad de Alzheimer mediante fMRI, Transformada Census Modificada y Clasificación Jerárquica.

Verónica Hernández Ramírez[1], Juan José Cárdenas Cornejo[1], Alan Ortega-Gonzalez[1], Yair A. Andrade-Ambriz[1], Mario-Alberto Ibarra-Manzano[1]

[1] Engineering Division, Campus Irapuato-Salamanca, University of Guanajuato, Salamanca, Guanajuato, México.
v.hernandez.ramirez@ugto.mx, jj.cardenasc@ugto.mx, a.ortegagonzalez@ugto.mx, ya.andrade@ugto.mx, ibarram@ugto.mx@ugto.mx

Abstract

Alzheimer's disease (AD) is the most prevalent neurodegenerative disorder worldwide, accounting for approximately 60–80% of dementia cases among older adults. Early detection of AD is particularly important because pathological brain changes may appear years or even decades before clinical dementia onset. This prodromal stage, commonly referred to as mild cognitive impairment (MCI), is marked by subtle memory and attention deficits, while patients largely retain functional independence. Consequently, identifying individuals at this stage may enable timely therapeutic interventions to delay disease progression and improve quality of life. Although several biomarkers have been proposed for AD diagnosis, including cerebrospinal fluid analysis and blood biomarkers, functional magnetic resonance imaging (fMRI) offers a promising noninvasive alternative for detecting disease-related functional alterations.

This study proposes a computer-aided framework for early detection of Alzheimer's disease using fMRI data. The methodology integrates slice selection, feature extraction, and machine learning classification to identify the brain regions that best characterize disease progression. First, the ReliefF algorithm ranks and selects the most discriminative fMRI slices. Next, the Modified Census Transform (MCT) and a set of statistical descriptors extract features that capture local functional patterns associated with AD. These features are then used to train and evaluate two classification schemes: a multiclass classifier that discriminates among healthy controls, prodromal subjects, and patients diagnosed with Alzheimer's dementia, and a hierarchical classifier composed of two consecutive binary stages.

Experimental results showed that the multiclass approach achieved classification accuracies ranging from 78.7% with a single slice to 89.5% when 16 selected slices were analyzed. To improve discrimination among clinically similar stages, we implemented a hierarchical framework: the first stage differentiates healthy subjects from those with Alzheimer's-related pathology, and the second stage differentiates prodromal patients from those diagnosed with Alzheimer's dementia. This hierarchical strategy significantly improved performance, achieving accuracies from 93.5% with a single slice to 99.6% with 16 selected slices.

These results demonstrate that combining ReliefF-based slice selection, Modified Census Transform feature extraction, and hierarchical classification yields an accurate, robust, and computationally efficient framework for early detection of Alzheimer's disease. Furthermore, the findings indicate that a small number of carefully selected slices can achieve highly competitive performance, highlighting the proposed methodology's potential as a non-invasive biomarker and a computer-aided diagnostic tool for early Alzheimer's disease assessment.

Index Terms— Alzheimer's disease, early diagnosis, functional magnetic resonance imaging (fMRI), Modified Census Transform, ReliefF, hierarchical classification, machine learning, neurodegenerative diseases.

1.Introduction

Alzheimer's disease (AD) is the most prevalent neurodegenerative disorder among older adults worldwide, accounting for 60% to 80% of diagnosed cases of clinical dementia (Sharma & Mandal, 2022). Contemporary

pathological research has demonstrated that the origin and biological progression of AD are intrinsically linked to the abnormal aggregation of extracellular βinicio ecuación menosamyloid plaques and intracellular neurofibrillary tangles composed of hyperphosphorylated tau protein; this process triggers massive synaptic degeneration and progressive neuronal atrophy, typically beginning in the entorhinal cortex and medial temporal lobe structures—most notably the hippocampus (Vrahatis *et al*., 2023; Wang *et al*., 2025a). AD falls within a broader clinical spectrum of neurodegenerative disorders that includes Lewy body dementia, frontotemporal dementia, and Parkinson's disease. According to the standardized criteria of the National Institute on Aging and the Alzheimer's Association (NIA-AA), the pathological progression is classified along a continuum comprising three major stages: the asymptomatic preclinical phase, Mild Cognitive Impairment (MCI)—subdivided into early MCI (EMCI) and late MCI (LMCI)—and active Alzheimer's dementia across mild, moderate, and advanced stages (Pandey *et al*., 2026). During the prodromal or MCI phase, timely detection is highly complex, as the initial manifestations—such as episodic short-term memory lapses, transient spatial disorientation, mood changes, and subtle alterations in fine motor skills—are nonspecific and frequently misattributed to normal biological aging or depressive disorders (Rehman *et al*., 2024). Empirical evidence indicates that pathological deposits and microstructural changes precede cognitive deficits by up to two decades (Ogu *et al*., 2024). Although there is currently no definitive cure for AD, early detection and multidisciplinary therapeutic intervention can significantly slow decline and substantially improve quality of life for both the patient and their family (Arafa *et al*., 2022).

The conventional clinical diagnosis of AD has historically relied on neuropsychological and cognitive screening tests—such as the Mini-Mental State Examination (MMSE) and the Clinical Dementia Rating (CDR)—complemented by clinical histories and detailed neurological examinations (Mahapatra & Selvakumar, 2025). However, these assessments show considerable inter-observer variability, are influenced by the subject's education level, and—crucially—detect damage only after neuronal death and synaptic dysfunction reach an irreversible threshold. In this context, non-invasive neuroimaging modalities—specifically structural Magnetic Resonance Imaging (sMRI), resting-state functional MRI (rs-fMRI), and Positron Emission Tomography (PET)—have become indispensable diagnostic tools, enabling in vivo examination of morphological changes, cortico-cortical disconnection, and reduced cerebral glucose metabolism (Ali *et al*., 2025; Hu *et al*., 2025). The establishment of multinational open-access initiatives, such as the Alzheimer’s Disease Neuroimaging Initiative (ADNI) and the Open Access Series of Imaging Studies (OASIS), has decisively advanced biomedical research by providing standardized, comprehensive repositories of longitudinal neuroimaging data, phenotypic information, and genetic profiles (Almalki *et al*., 2024; Kung *et al*., 2026). Researchers have developed various processing frameworks based on these databases. Initially, classical machine learning (ML) models relied on the manual extraction of volumetric and morphometric features; for example, (Ahmad *et al*., 2023) applied a framework based on Principal Component Analysis (PCA) and Stepwise Linear Discriminant Analysis (SWLDA) to feed artificial neural networks, achieving 98.7% accuracy in binary discrimination and 96.5% in separating four stages, thereby highlighting the feasibility of using compact statistical representations to mitigate overfitting. In parallel, (Mahapatra & Selvakumar, 2025) employed nonlinear mathematical models and SHAP-interpretable supervised classifiers on the OASIS-1 dataset, demonstrating 94.20% accuracy and confirming that ventricular volume is a decisive geometric biomarker. Likewise, the exploration of low-cost, easily accessible behavioral biomarkers in primary care has gained prominence: (Mitra & Rehman, 2024), along with Rehman and Mitra (2025), reported accuracies exceeding 92% by analyzing kinematic and pressure dynamics in handwriting using SVM and Random Forest, while (Govindarajan *et al*., (2026) demonstrated via the NeuroCognex platform that spectral analysis of electroencephalographic (EEG) signals enables the detection of prodromal functional disconnection with 95.40% accuracy.

Despite significant advances in classical machine-learning-based analytics, Deep Learning (DL) has radically transformed the landscape by enabling autonomous extraction of complex hierarchical representations from MRI scans, eliminating the need for manual segmentations prone to bias. (Muksimova *et al*., 2025) developed a Convolutional Neural Network (CNN) enhanced with spatial and channel attention mechanisms (CBAM), achieving 98.92% diagnostic accuracy in four-stage categorization using the ADNI dataset. Focusing on efficiency for resource-constrained computing devices, (Ullah *et al*., 2026) introduced LADNET—a lightweight architecture employing depthwise separable convolutions and dense residual connections—which achieved 99.15% accuracy in binary discrimination and 97.80% in multi-stage classification, while reducing the parameter count by over 65% compared to traditional networks. Similarly, to address recurring inter-subject data leakage, (Sifat *et al*.,2026) implemented a multi-channel volumetric 3D CNN with strict patient-level evaluation, reporting 96.10% balanced accuracy and establishing a rigorous methodological standard for clinical validation. Other notable convolutional approaches include work by (Chabib & Hadjileontiadis, 2023), who integrated the Curvelet Transform (DeepCurvMRI) to preserve subtle curvilinear cortical edges (96.84% accuracy); Alsubaie (2024), who designed ConvADD using dilated convolutions, achieving 97.20%;

(Ghahramani *et al*., 2026), who utilized CortexNet to harmonize 1.5T and 3.0T scans (98.12%); and (Hassan *et al*., 2025), who combined multi-channel stacked convolutional networks to simultaneously extract sagittal, coronal, and axial planes, achieving 98.40% accuracy. Complementarily, hybrid schemes—such as the one formulated by (Zolfaghari *et al*., 2025)—connected a dual parallel CNN with a machine learning ensemble (SVM, Random Forest, and k-NN) optimized via grid search, achieving 97.45% accuracy; this confirms that the convergence of deep convolutional descriptors and machine learning margin-based classifiers optimizes the decision boundary during transition phases such as MCI.

In recent years, the Vision Transformer (ViT) paradigm and global attention mechanisms have gained prominence by overcoming the intrinsic limitation of the local receptive field in standard convolutions. (Ahmed, 2025) demonstrated that enriching grayscale MRI scans with pseudo-RGB chromatic projections optimizes Vision Transformer attention, achieving 99.04% accuracy in multi-class classification. Meanwhile, (Wang *et al*., 2025b) proposed a cooperative scheme that integrates local convolutions with the shifted-window Swin Transformer, reporting 97.85% accuracy in capturing long-range interhemispheric morphological correlations. Along similar lines, (Odusami *et al*., 2023) applied pixel-level fusion alongside ViT, achieving 99.20% on the OASIS dataset; (Zhang *et al*., 2025) formulated the DA-ViT transformer with deformable attention (98.35% accuracy), dynamically adapting sampling to irregular atrophic geometries; and (Ibrar *et al*., 2025) designed a network featuring inverted residual bottlenecks and self-attention (98.60% accuracy). Additionally, (Kannan *et al*., 2026) combined ConvTransformer blocks with adaptive Squeeze-and-Excitation attention (98.70%), while (Leelavathi *et al*., 2026) developed a cloud-deployed hybrid CNN-Transformer framework with 40% lower inference latency, facilitating large-scale clinical telediagnosis. Beyond univariate neuroimaging, the multimodal fusion of imaging data with genetic profiles (particularly the APOE-ε4 allele), cerebrospinal fluid (CSF) data, and cognitive test results has opened decisive new frontiers. (Yu *et al*., 2024) formulated a unified multimodal transformer with cross-attention to correlate sMRI, FDG-PET, and genetic data, achieving an AUC of 0.984 for diagnosis and 0.892 for the prospective prediction of conversion from MCI to AD at 24 months. In a fundamental advance in biomolecular integration, (Wang *et al*., 2025a) showed that coupling genetic variants (SNPs) with sMRI allows correlation of deep attention maps with known biological pathways of neurodegeneration ($R^2=0.84$ with MMSE). (Tan *et al*., 2026) introduced novel Kolmogorov-Arnold Networks (KANs) to replace traditional multilayer perceptrons, generating interpretable models based on univariate non-linear functions with 97.35% accuracy. Other relevant multimodal frameworks include (Gupta *et al*., 2025), using lightweight late-fusion networks combining sMRI and CDR/MMSE scales (98.10%); (Rahman *et al*., 2025), integrating sMRI and DTI tractography via NeuroNet-AD (97.85%); and (Alorf, 2025), who formulated a balanced CNN-Transformer gradient approach using tabular biomarkers and images (98.15%). To mitigate the "black box" problem and ensure clinical reliability, (Al-bakri *et al*., 2025) implemented the HXAI hybrid framework, incorporating radiological validation via Grad-CAM++ and SHAP maps (97.50%); (Zubair *et al*., 2025) integrated preliminary U-Net segmentation with XAI (98.65%); (Abubakr *et al*., 2026) formulated an attention-based federated learning scheme that safeguards decentralized hospital privacy (96.85%); and (Lee & Lee., 2026) designed a cross-population transfer learning strategy to adapt models trained on ADNI for small Asian cohorts, addressing demographic bias with an 11.4% performance increase.

Despite these achievements, critical limitations persist in the state of the art: 1) most high-performance models incur prohibitive computational costs due to the use of full 3D volumes or oversized transformers; 2) there is a high susceptibility to overfitting and data leakage during slice-based partitioning; and 3) accurately distinguishing the early prodromal stage (EMCI) from healthy aging continues to yield significant error margins when assessed in isolation. To address these issues, this study proposes a comprehensive strategy based on MRI processing and machine learning algorithms optimized for Alzheimer's detection and staging. The methodology's key aspects are structured as follows: 1) early and prodromal phase detection proves highly efficient, demonstrating that the disease can be categorized with high fidelity using a select subset of representative slices—obtained through morphological filtering and dimensionality reduction—achieving over 95% accuracy and highlighting the viability of a computationally lightweight approach; 2) exhaustive analysis of multiple slices does not always yield proportional improvements, as indiscriminate increases in input volume raise latency and spatial redundancy without significantly boosting diagnostic sensitivity; and 3) a relevance-guided selection and ensemble strategy offers the optimal balance between computational cost, clinical interpretability, and accuracy, thereby maximizing the system's overall performance.

This research aims to develop non-invasive computational biomarkers for early detection of Alzheimer's disease using functional magnetic resonance imaging (fMRI). The proposed framework integrates ReliefF-based slice selection, Modified Census Transform (MCT) feature extraction, statistical descriptors, and machine learning classifiers to identify functional alterations associated with the disease, particularly in its prodromal stage. Experimental results demonstrate that the proposed hierarchical classification strategy significantly improves discrimination among clinical states, achieving up to 99.6% accuracy while maintaining low computational complexity. These findings suggest that the proposed methodology is a promising

computer-aided diagnostic tool for supporting early Alzheimer's disease assessment. The following sections present the proposed methodology, experimental setup, results, discussion, and conclusions.

2. Proposed Methodology

This paper proposes a methodological approach for classifying and detecting three stages of AD using functional magnetic resonance imaging (fMRI) data. The study uses data from the ADNI dataset to evaluate machine learning algorithms for distinguishing among healthy subjects (E1: CN), individuals in the early stage or with mild cognitive impairment (E2: MCI), and patients diagnosed with Alzheimer's dementia (E3: AD).

Figure 1 illustrates the developed methodology. The process begins with database analysis and preparation to select the most representative images for each category, a crucial step to reduce classification bias and highlight the textural and structural nuances in brain images that are characteristic of each phase.

Subsequently, two parallel data-balancing schemes are implemented:

1. **Balancing Scheme 1:** Focuses on applying the Modified Census Transform (MCT) and computing statistical features to build a feature matrix. Two main processes are derived from this matrix:
   - **fMRI slice filtering:** From the 49 axial slices comprising the fMRI volume, the Relief algorithm is applied to select only the most relevant and representative slices.
   - **Multiclass classification:** A multiclass classifier designed to discriminate among the three patient states (E1, E2, and E3) is directly evaluated.
2. **Balancing Scheme 2:** Following the selection of the optimal set of slices via ReliefF, the attributes representative of the condition feed into a hierarchical classification architecture with two sequential stages:
   - **Stage 1 (Classifier 1):** Evaluates whether the subject is healthy (E1) or has the condition, grouping patients from stages E2 and E3 into a single category (Patients).
   - **Stage 2 (Classifier 2):** If the subject is identified as having the disorder, a specific distinction is made between E2 and E3 to determine the final diagnosis of the condition.

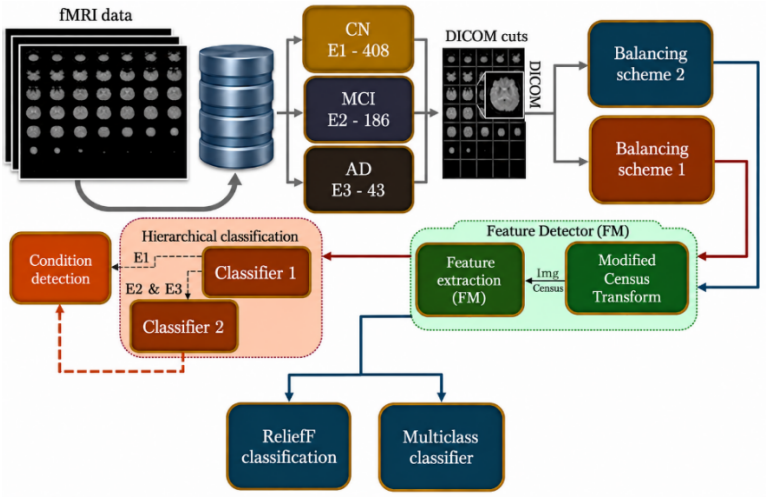


Figure 1. Proposed methodology.
Source: Own authorship

2.1. Image acquisition

To develop the proposed methodology, a cohort of 637 samples was selected from the ADNI database, distributed across three clinical stages: 408 samples for E1, 186 for E2, and 43 for E3. Each fMRI sample is stored in DICOM format and consists of a sequence of 210 temporal frames with a resolution of 468 × 468 pixels. Each frame comprises 49 axial slices capturing Blood Oxygen Level Dependent (BOLD) signal

variations across the brain structures of interest, reflecting the standard fMRI acquisition structure for the corresponding diagnostic stage (E1, E2, E3).

Given the marked class imbalance in the available sample volume, we proposed two balancing schemes (Figure 1) to equalize the number of samples across categories, using the number of frames from the majority class (E_1) as a reference. All classifiers receive the same information during evaluation to ensure an objective, comparable analysis.

In Balancing Scheme 1 in Figure 1, the ReliefF algorithm identified the fMRI slices with the greatest clinical relevance; of the original 49 slices, 7 were qualitatively discarded for lacking discriminative information, leaving 42 slices for ReliefF analysis, from which the 16 most significant were selected. Based on this selection, various randomly generated combinations were evaluated to measure the accuracy of a multiclass classifier: first, the individual capability of each of the 42 slices was assessed; subsequently, random subsets of 2^n slices ($within = 4$) drawn from those selected by ReliefF were formed for processing during the preprocessing and classification stages. Separately, Balancing Scheme 2 was designed to feed a hierarchical classification framework: an initial binary phase distinguishes between (E_1 vs. $E_2 + E_3$), while the second phase evaluates clinical progression exclusively (E_2 vs E_3). This combined approach integrating slice selection and sampling strategies significantly optimized pathological pattern detection and overall model performance.

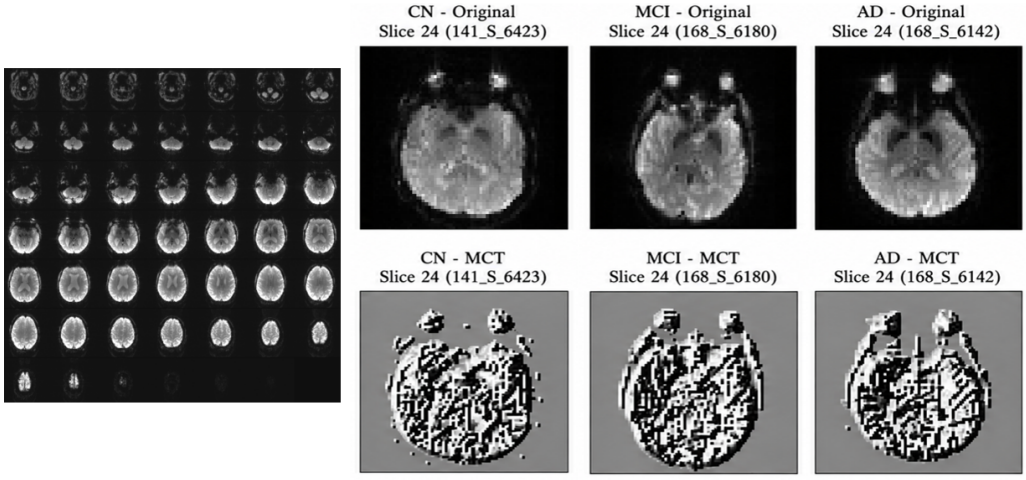


Figure 2. Full-volume fMRI and axial slices (Slice 24) for CN (E1), MCI (E2), and AD (E3): Original vs. CTM-processed representation. Source: Own authorship

2.2. Feature extraction

The MCT is a non-parametric variant designed to extract texture features from grayscale images (Fröba & Ernst, 2004). It evaluates the local spatial structure within a designated analysis window by comparing neighboring pixel intensities against thresholds derived from the region itself. This procedure generates binary strings that are subsequently concatenated and converted from fixed-point to decimal representation, as illustrated in Figure 3.

The process shown in the figure begins by establishing an analysis window (ws) in this demonstration, a $[3 \times 5]$ window (ws) applied to the analysis matrix (AM), which in this project corresponds to the fMRI pixel matrix. The center pixel of this window is selected as the reference pixel. Unlike the CT, which evaluates the neighborhood by comparing each pixel solely against the discrete value of the center pixel, the MCT algorithm generates two reference thresholds based on the window's characteristics: an upper threshold, $C_{rs} = ws + s_w$, and a lower threshold, $C_{ri} = ws - s_w$ as shown in Equation (1).

Using these thresholds, the algorithm evaluates two binary substrings in parallel:

- **Upper substring (C_s):** Assigns a value of "1" to positions (m, n) where the intensity $ws_{(m,n)}$exceeds the threshold C_{rs} ("true"=1, "false"=0), producing a binary vector such as 10001000000010.
- **Lower substring (C_i):** Assigns a value of "1"when the intensity $ws_{(m,n)}$ is lower than the threshold $C_{ri}("true" = 1, "false" = 0)$, yielding the corresponding binary vector [00000100100000]. Next, the two sequences are combined via concatenation (joining arrays), producing a structured feature string (14-bit MCT string) denoted in matrix form as $Mc_{(i,j)}$. Finally, a dot product of the binary arrays maps the encoded information to a matrix of decimal MCT results.

This conceptual difference is MCT's primary advantage over classical CT: by not relying rigidly and exclusively on the central pixel intensity, MCT mitigates the impact of noise and acquisition artifacts. This modification imparts greater stability, immunity to local illumination variations, and superior discriminative power for complex pattern analysis.

$$\xi(w_s, c_s, c_i) \equiv \begin{cases} \mathbb{C}_s = \begin{cases} 1, & \text{if } w_s(x) > c_s \\ 0, & \text{Otherwise} \end{cases} \\ \mathbb{C}_i = \begin{cases} -1, & \text{if } w_s(x) < c_i \\ 0, & \text{Otherwise} \end{cases} \end{cases} \tag{1}$$

where $\xi(\cdot)$represents the ternary sequence generated from the neighborhood analysis, consisting of $[(r \times c) - 1]$elements (14 elements for example shown in Figure 3. The final $MCT(x)$ value is then obtained through a 2^n-dimensional weighting scheme that converts the ternary sequence into a fixed-point numerical representation as shown in Figure 3. This encoding captures local image intensity variations by incorporating relationships between the central pixel and its neighbors under the tolerance constraints established within the analysis window. The parameter $n$is defined as $\left\{n \middle| \in \middle| \mathbb{R} \quad -\left\lfloor \frac{r \times c}{2} \right\rfloor \leq n \leq \left\lfloor \frac{r \times c}{2} \right\rfloor \; n \neq 0 \right\}$, as expressed in:

$$MCT(x) = 2^n \otimes \xi(w_s, c_s, c_i) \tag{2}$$

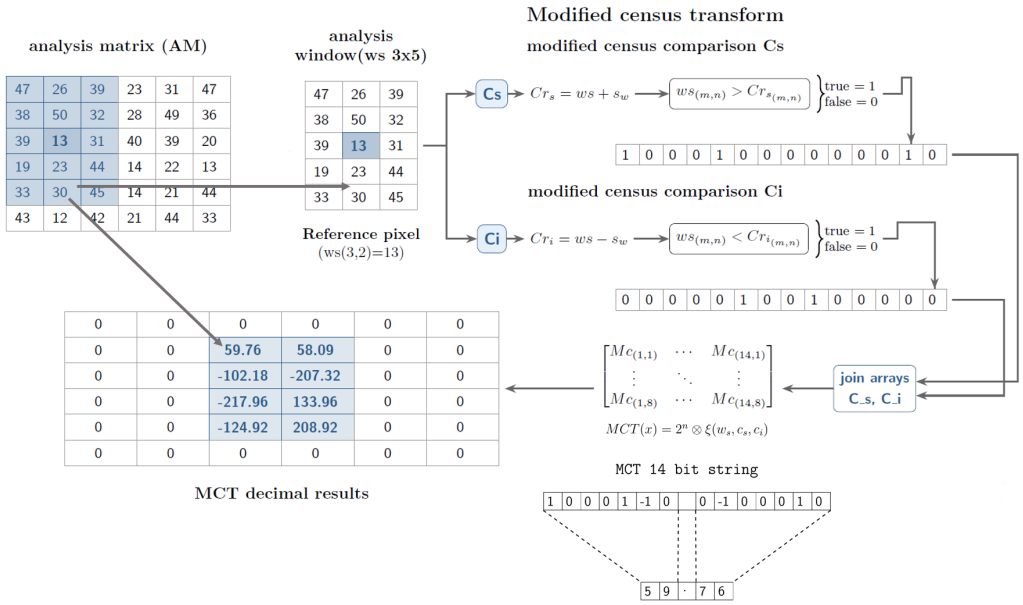


Figure 3. Schematic representation of the Modified Census Transform (MCT) feature extraction, local binary pattern encoding, and upper/lower threshold decomposition on axial fMRI slices.
Source: Own authorship

2.3. Experimental Configuration

The proposed methodology, illustrated in Figure 1, was developed using fMRI sequences from the ADNI database to identify discriminative patterns associated with different stages of Alzheimer's disease. The final dataset consisted of 637 samples distributed into three diagnostic categories: 408 samples belonging to E1, 186 subjects belonging to E2, and 43 subjects belonging to E3.

Each sample was represented by a functional acquisition composed of 210 frames stored in DICOM format. Each frame had a spatial resolution of $[468 \times 468]$ pixels and contained 49 consecutive axial brain slices. Because the ADNI database integrates studies acquired with different scanners and imaging protocols, we standardized the data to reduce scanner-related variability. Consequently, we considered only studies acquired using the Siemens Magnetom Trio 3T scanner. We selected this protocol because it provided the most available samples, particularly for subjects in the early stages of the disease.

Unlike conventional approaches that exploit the complete temporal information available in fMRI acquisitions, the proposed methodology does not perform a spatio-temporal analysis. Instead, a single functional frame was selected from each subject, and all subsequent analyses were conducted using the spatial information contained within that frame. This strategy enabled characterization of local variations in the BOLD signal while significantly reducing the computational complexity of processing complete fMRI sequences.

Next, we independently extracted and resized the 49 axial slices in each frame to $[66 \times 66]$ pixels. Preliminary inspection revealed that the central slices contained a larger proportion of brain tissue and a lower presence of extracerebral regions. Therefore, 40 central axial slices were initially selected for further analysis. We evaluated each slice independently throughout the experimental process to determine its contribution to discriminating against ADstages.

Because the dataset showed pronounced class imbalance, we implemented an initial balancing strategy during feature extraction and selection. This scheme was designed to evaluate each slice's discriminative capability using the ReliefF algorithm. The procedure used the majority class as a reference and applied controlled oversampling by randomly selecting functional frames from each subject.

Each sample is represented by a sequence of 210 functional frames acquired at different time points. Therefore, the randomly selected frames do not correspond to exact replicas but rather to distinct observations of the subject's functional brain activity. This characteristic allows us to generate additional observations while preserving the natural variability of the BOLD signal.

The balancing factors assigned to each diagnostic category were defined as:

$$F_1 = 2,\ F_2 = 2,\ F_3 = 9 \tag{3}$$

Where F_c represents the data rebalancing factor associated with class c. The effective number of observations after balancing was computed as:

$$N_c' = N_c \times F_c \tag{4}$$

resulting in:

$$\begin{aligned} N_1' &= 816, \\ N_2' &= 372, \\ N_3' &= 387. \end{aligned} \tag{5}$$

This procedure substantially reduced class imbalance and produced a more uniform representation for subsequent feature extraction and selection.

After balancing, we processed each axial slice with the MCT. This transformation aimed to highlight local texture variations potentially associated with functional alterations caused by Alzheimer's disease. The MCT descriptor captures local spatial relationships among neighboring pixels and provides a robust representation of intensity variations in the BOLD signal.

Subsequently, we extracted a set of statistical descriptors from each transformed image to characterize the distribution of the generated patterns. Let

$$f_i = [f_{i1}, f_{i2}, \ldots, f_{id}] \tag{6}$$

denote the feature vector extracted from the i-th observation, where d represents the total number of calculated attributes. The concatenation of all feature vectors forms the feature matrix:

$$F \in \mathbb{R}^{n \times d} \tag{7}$$

Where n corresponds to the total number of observations available after the balancing process.

We used the resulting feature matrix as input to the ReliefF algorithm, which assigns a relevance score to each slice based on its ability to discriminate among diagnostic categories. We considered slices with the highest relevance scores the most informative and selected them for the classification stage. The feature matrices generated from these selected slices were evaluated with a multiclass classifier designed to discriminate among the three diagnostic categories simultaneously.

Additionally, we proposed a hierarchical classification strategy with two consecutive binary stages. The primary motivation behind this strategy was to progressively simplify the classification problem by first separating $E1$ from $E2 + E3$ and subsequently distinguishing between pathological stages $E2 + E3$.

In the first stage, E2 and E3 were grouped into a single pathological category, while E1 remained an independent category. This grouping can be mathematically expressed as:

$$E = E_1 \tag{8}$$

and

$$E_P = E_2 \cup E_3 \tag{9}$$

Where E_N represents the normal category and $E_P$represents the pathological category.

To balance both categories, a second balancing scheme was implemented using the following factors:

$$F_1 = 1,\ F_2 = 1,\ F_3 = 5. \tag{10}$$

As a result, the following numbers of observations were obtained:

$$\begin{aligned} E_1' &= 408, \\ E_2' &= 186, \\ E_3' &= 215. \end{aligned} \tag{11}$$

Consequently, the pathological category contained:

$$E_P' = E + E = 401 \tag{12}$$

observations, whereas the normal category contained:

$$E_1' = 408 \tag{13}$$

observations. This configuration generated nearly equivalent class distributions during the first stage of the hierarchical classifier.

After identifying subjects as belonging to the pathological group, we performed a second binary classification stage using only samples corresponding to $E2$ and $E3$. For this stage, we maintained the same balancing factors, resulting in 186 observations for E2 and 215 observations for E3. Therefore, the feature matrices employed in both stages of the hierarchical framework remained approximately balanced.

A fundamental aspect of the proposed methodology is that all classifiers evaluated throughout the study received the same feature representation, were trained on feature matrices constructed from the same selected slices, and operated on equivalent amounts of information per class. Consequently, differences in classification performance can be attributed to the discriminative capability of the classifiers rather than to variations in data availability or sample distribution. This strategy ensures a fair, objective, and unbiased comparison among all evaluated classification models.

After defining the balancing schemes and selecting the most representative slices, we evaluated different spatial configurations to analyze local BOLD signal variations using the proposed descriptor. For this purpose, seven neighborhood window sizes were considered:

$$w_s = \{(3 \times 3), (3 \times 5), (5 \times 5), (5 \times 7), (7 \times 7), (7 \times 9), (9 \times 9)\}. \tag{14}$$

Each window defines a local neighborhood centered on the reference pixel and enables analysis of spatial relationships between that pixel and its neighbors. The selected window sizes were designed to evaluate multiple spatial scales while preserving sensitivity to local intensity variations within the $[66 \times 66]$ axial slices.

Smaller windows emphasize fine-grained details and local intensity transitions, whereas larger windows incorporate additional contextual information from neighboring regions. However, the maximum window size

was restricted to $[9 \times 9]$ because excessively large neighborhoods tend to smooth local variations and reduce the discriminative capability of the descriptor. As the neighborhood size increases, local intensity transitions around the reference pixel may become diluted, potentially decreasing sensitivity to subtle functional alterations associated with Alzheimer's disease.

Therefore, the proposed window configurations (w_s)enabled analysis of local BOLD signal characteristics at multiple spatial scales and facilitated identification of the neighborhood size that provides the most discriminative representation of Alzheimer's disease-related functional alterations.

2.4. Feature extraction

The proposed feature extraction framework was developed to identify attributes capable of discriminating among different stages of AD using fMRI. Each sample consists of a sequence of 210 consecutive axial slices with a spatial resolution of $[66 \times 66]$ pixels. Rather than performing spatiotemporal analysis on the full sequence, we conducted statistical analysis on individual slices or groups of previously selected slices. This strategy significantly reduces computational complexity while preserving the most relevant disease-related information.

First, the ReliefF algorithm selects the most representative slices. Next, we process each slice using the MCT, which enhances local image patterns and helps extract information relevant to the neurological conditions under study. After applying the MCT, we performed a window-based analysis using seven analysis windows, allowing us to extract local information from different regions of the transformed image.

For each analysis window, we compute eight statistical and shape descriptors from the coefficients obtained via the MCT. Specifically, the descriptors are the mean, variance, median, first quartile, third quartile, minimum, maximum, and the vertex position of a parabola fitted to the histogram of the transformed coefficients. The first seven describe central tendency, dispersion, and distribution, whereas the last provides information about the overall shape of the distribution. The vertex position is computed as

$$\mathrm{x_v} = -\frac{\mathrm{b}}{2\mathrm{a}} \tag{15}$$

where a and b represent the coefficients of the second-order polynomial fitted to the histogram of the MCT coefficients. Collectively, these descriptors provide a compact and highly discriminative representation of each analyzed window.

The dimensionality of the feature matrix depends on the number of available samples, the number of analyzed slices, the number of analysis windows per slice, and the number of extracted descriptors per window. In general, the dimensionality of the feature matrix is defined by Equation (X):

$$Dim(M_f) = [N,\ (C \cdot W \cdot F) + 1] \tag{16}$$

where N denotes the number of samples, C the number of analyzed slices, W the number of analysis windows, F the number of extracted descriptors per window, and the additional term corresponds to the class label vector.

In this study, $N = 1575$ samples, $W = 7$ analysis windows, and $F = 8$ descriptors per window were employed. For the case of a single axial slice ($C = 1$), the dimensionality of the feature matrix is obtained as

$$Dim(M_f) = [1575,\ (1 \cdot 7 \cdot 8) + 1] = [1575, 57] \tag{17}$$

Therefore, the feature matrix used to represent a single slice has dimensions of 1575×57.

When 16 axial slices are analyzed simultaneously ($C = 16$), the dimensionality of the feature matrix is given by.

$$Dim(M_f) = [1575,\ (16 \cdot 7 \cdot 8) + 1] = [1575, 897] \tag{18}$$

Consequently, the feature matrix used by the classifiers has dimensions of 1575×897.

To ensure an objective and reproducible comparison, all classifiers evaluated in this study receive exactly the same information during the training, validation, and testing stages. Consequently, any differences observed in classification performance can be attributed exclusively to the learning and discrimination capabilities of the classifiers rather than to variations in the input data. The only variable modified across experiments is the number of axial slices used to construct the feature matrix, allowing a systematic evaluation of the contribution of additional spatial information from multiple consecutive slices.

Figure 1 illustrates the complete processing pipeline, including slice selection using ReliefF, feature extraction through the MCT, computation of the statistical and shape descriptors, and construction of the final feature matrix used as input to the classification models.

2.5. Classifiers and Validation Strategies

Once the feature matrices described in the previous section were constructed, their discriminative capability was evaluated using the classifiers available in the Classification Learner Toolbox of MATLAB. We analyzed 25 supervised classifiers from different machine learning families, including decision trees, discriminant analysis methods, support vector machines (SVMs), k-nearest neighbors (KNN), probabilistic classifiers, and ensemble methods.

To ensure an objective, reproducible, and unbiased comparison, we trained and evaluated all classifiers using the same feature matrices. We also kept each model's hyperparameters at MATLAB's default values and did not perform further optimization. Consequently, any differences in classification performance can be attributed solely to the learning and generalization capabilities of the evaluated algorithms, rather than to changes in the input data or classifier configurations.

- **Multiclass Classification:** Initially, the problem was addressed as a multiclass classification task considering the three clinical states simultaneously: E1, E2, and E3. For this purpose, a feature matrix with dimensions of $[1567 \times 57]$ was constructed, where the first 56 columns correspond to the descriptors extracted through the MCT and the last column contains the class label. This dimensionality resulted from combining a simple axial slice, seven analysis windows, and eight statistical and shape descriptors per window. To reduce the impact of class imbalance, we implemented a balancing scheme using balancing factors of 1, 2, and 9 for classes E1, E2, and E3, respectively. We validated the model using MATLAB's Holdout Validation scheme, using 80% of the samples for training and the remaining 20% for validation.
- **Hierarchical Classification:** In addition to the multiclass approach, we proposed a hierarchical classification strategy composed of two consecutive binary classifiers. The complete database consisted of $1{,}575$ samples distributed among three classes: $E1, E2$, and $E3$. In the first stage, a binary classifier was trained to discriminate between samples from class $E1$ and those from classes $E2$ and $E3$ grouped into a single category. This stage involved 816 samples from class $E1$, and a second group composed of 372 samples from class $E2$ and 387 samples from class $E3$. Therefore, the first level of the hierarchical classifier performs the following discrimination: $E1$ vs. $(E2 + E3)$. After this stage, samples classified within the second group are passed to a second binary classification stage, where discrimination between classes $E2$ and $E3$ is performed: $E2$ vs. $E3$. This second stage involves 372 samples from class $E2$ and 387 samples from class $E3$, providing a nearly balanced class distribution. Therefore, the overall hierarchical classification structure can be represented as: Stage 1: $E1$ vs. $(E2 + E3)$and Stage 2: $E2$ vs. $E3$. Additionally, to identify the most suitable hierarchical configuration, we evaluated all possible combinations of the 25 MATLAB classifiers across the two stages of the hierarchical framework. Because the same classifier could be used in both stages, we considered combinations with repetition. Thus, the total number of evaluated configurations was determined as $N_{comb} = N_c^2$, where $N_c$represents the number of available classifiers. Considering $N_c = 25$, the total number of hierarchical configurations becomes $N_{comb} = 25^2 = 625$. As a result, we evaluated 625 different hierarchical classifier configurations. For each configuration, we executed the full training, validation, and evaluation procedure. Because we analyzed so many combinations, the Results section reports only the configurations that achieved the highest classification performance.
- **Monte Carlo Validation Strategy:** Unlike the multiclass approach, we evaluated the hierarchical classifier using a Holdout validation strategy combined with Monte Carlo resampling. To do so, we generated 30 independent random partitions of the dataset while preserving the original class proportions in each iteration. We used each partition to run the full training and validation process, ensuring each run used different samples. We then computed the performance metrics as the mean and standard deviation across the 30 independent runs. This procedure reduces dependence on a single data partition and provides a more statistically robust and reliable estimate of classifier performance. Furthermore, the Monte Carlo validation framework enabled the systematic evaluation of different combinations of axial brain slices. This allowed us to analyze how additional spatial information from multiple consecutive slices contributes to classification performance, as illustrated in Figure 6. In summary, we evaluated 25 individual classifiers for the multiclass problem. We assessed 625 hierarchical configurations for the two-stage classification framework. All experiments

used identical training and validation conditions, MATLAB's default classifier parameters, and the same feature matrices for each evaluated configuration. This ensures consistent comparisons among algorithms and enables objective identification of the configurations with the highest discriminative capability for detecting different stages of Alzheimer's disease.

3.Results

Machine learning techniques have proven effective for analyzing fMRI data because they can identify complex patterns associated with alterations in brain activity. The BOLD signal contained in fMRI sequences provides indirect information about neuronal activity, enabling the study of functional changes related to neurodegenerative disorders such as Alzheimer's disease. Numerous studies show that machine learning models can detect changes in brain connectivity before the onset of clear clinical symptoms, making them a promising approach for early diagnosis.

In this work, the primary objective was to discriminate among three states associated with Alzheimer's disease, with particular emphasis on identifying state E2 because of its relevance to early diagnosis and timely intervention. To achieve this goal, the proposed methodology employed ReliefF-based slice selection, MCT, and the extraction of statistical and shape descriptors. This strategy characterizes local patterns in brain images and captures subtle variations associated with transitions among clinical states.

The proposed methodology analyzes local windows (ws) around each reference pixel. MCT highlights spatial patterns associated with changes in functional brain connectivity, while the extracted descriptors summarize the information in each analyzed region. As a result, each brain slice yields a compact, highly discriminative representation suitable for supervised classification algorithms.

To evaluate the discriminative capability of the extracted features, we analyzed two classification strategies. The first corresponds to a multiclass classification scheme in which classes $E1, E2$, and $E3$ are simultaneously discriminated against using the 25 classifiers available in the Machine Learning Toolbox of MATLAB R2020b. To ensure an objective and reproducible comparison, we evaluated all classifiers using the same feature matrix, the same training and validation partitions, and identical experimental conditions.

The second strategy uses a hierarchical classification framework that decomposes the multiclass problem into two consecutive binary classification stages. In this case, we evaluated all possible combinations of the 25 available classifiers, resulting in 625 hierarchical configurations. This approach lets each classification stage specialize in a specific discrimination task, facilitating the progressive identification of different clinical states.

Table 1 presents results for the multiclass and hierarchical classification schemes. For the hierarchical classifier, the reported results correspond to the average classification accuracy from 30 independent executions using the Monte Carlo validation scheme, along with the corresponding standard deviation. These metrics allow evaluation of not only each configuration's average performance but also its stability and robustness across different training and validation partitions.

For each experimental configuration, we analyzed different numbers of axial brain slices. Specifically, we evaluated sets composed of $1, 2, 4, 8$, and 16 slices selected through ReliefF. Because slice selection can significantly influence system performance, we considered three different slice combinations for each configuration. These combinations correspond to different subsets of slices that ReliefF identified as most representative of the disease, allowing us to analyze how both the number and spatial location of slices affect classification performance.

Table 1. *Performance results for multiclass and hierarchical classification schemes across different slice configurations.*

Slices	C1	C2	Accuracy	Precision			Accuracy classifier multiclass	
				E1	E2	E3		
2,4,7,9,11,15,18, 20,22,25,28,30,33,35,37,39	S-KNN	S-KNN	0.991±0.019	0.996±0.014	0.987±0.038	0.986±0.040	S-KNN	0.895
1,3,5,8,12,14,16,19,21, 24,27,29,31,34,38,40	S-KNN	S-KNN	0.993±0.014	0.997±0.012	0.987±0.032	0.990±0.029	S-KNN	0.875

6,10,13,15,17,20,22,23,26,28,30,32,35,36,37,39	S-KNN	S-KNN	0.994±0.015	0.993±0.021	0.997±0.013	0.995±0.024	S-KNN	0.879
3,8,14,19,22,28,33,37	S-KNN	S-KNN	0.989±0.020	0.986±0.032	0.992±0.029	0.993±0.027	S-KNN	0.889
5,11,16,21,25,30,34,39	S-KNN	S-KNN	0.992±0.015	0.988±0.024	0.995±0.026	1.000±0.000	S-KNN	0.893
2,9,15,20,26,31,35,40	S-KNN	S-KNN	0.993±0.014	0.994±0.018	0.990±0.031	0.995±0.024	S-KNN	0.803
7,18,27,36	S-KNN	S-KNN	0.978±0.023	0.981±0.030	0.981±0.038	0.974±0.049	S-KNN	0.811
4,13,23,32	S-KNN	S-KNN	0.968±0.027	0.970±0.034	0.966±0.053	0.971±0.059	S-KNN	0.823
10,17,29,38	S-KNN	S-KNN	0.975±0.034	0.981±0.030	0.981±0.038	0.974±0.049	S-KNN	0.815
12,28	KNN-F	S-KNN	0.940±0.036	0.952±0.039	0.910±0.079	0.951±0.058	SVM	0.796
19,35	KNN-F	S-KNN	0.943±0.038	0.953±0.036	0.913±0.082	0.957±0.053	F-KNN	0.803
8,24	S-KNN	S-KNN	0.961±0.027	0.968±0.038	0.953±0.051	0.960±0.052	SVM	0.776
36	KNN-F	S-KNN	0.915±0.039	0.928±0.048	0.895±0.087	0.919±0.066	F-KNN	0.756
24	KNN-F	S-KNN	0.908±0.044	0.920±0.052	0.869±0.089	0.937±0.074	F-KNN	0.749
29	KNN-F	S-KNN	0.906±0.042	0.935±0.040	0.874±0.077	0.894±0.079	F-KNN	0.787

Source: Own authorship

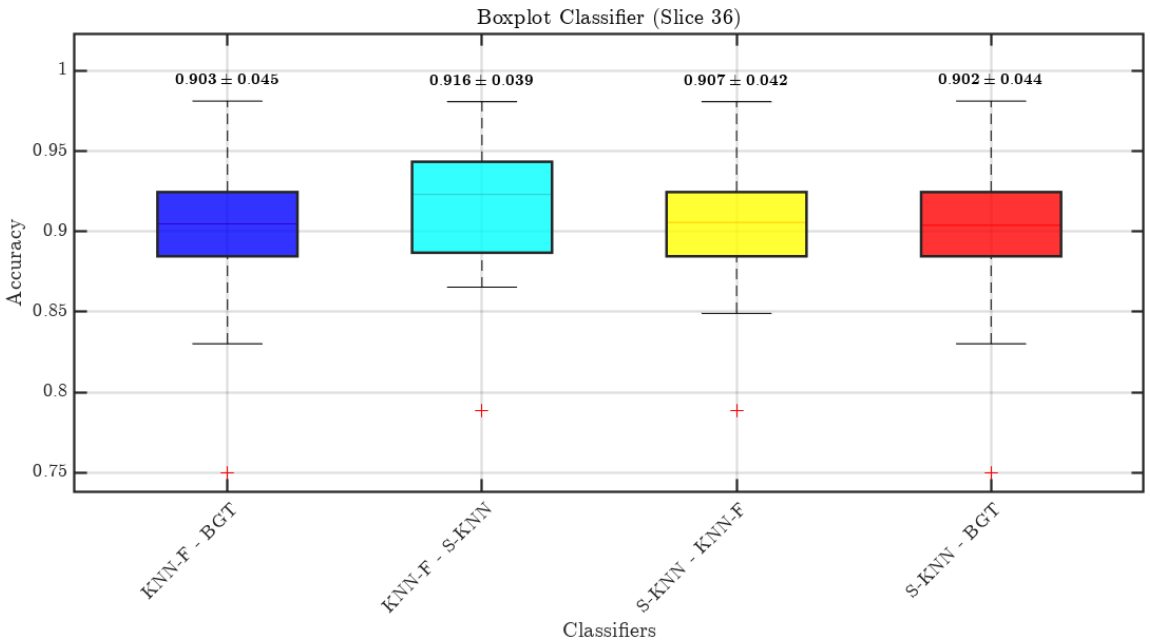


Figure 4. Multiclass classification accuracy and F1-score performance across evaluated feature descriptors and ReliefF axial slice selection configurations.
Source: Own authorship

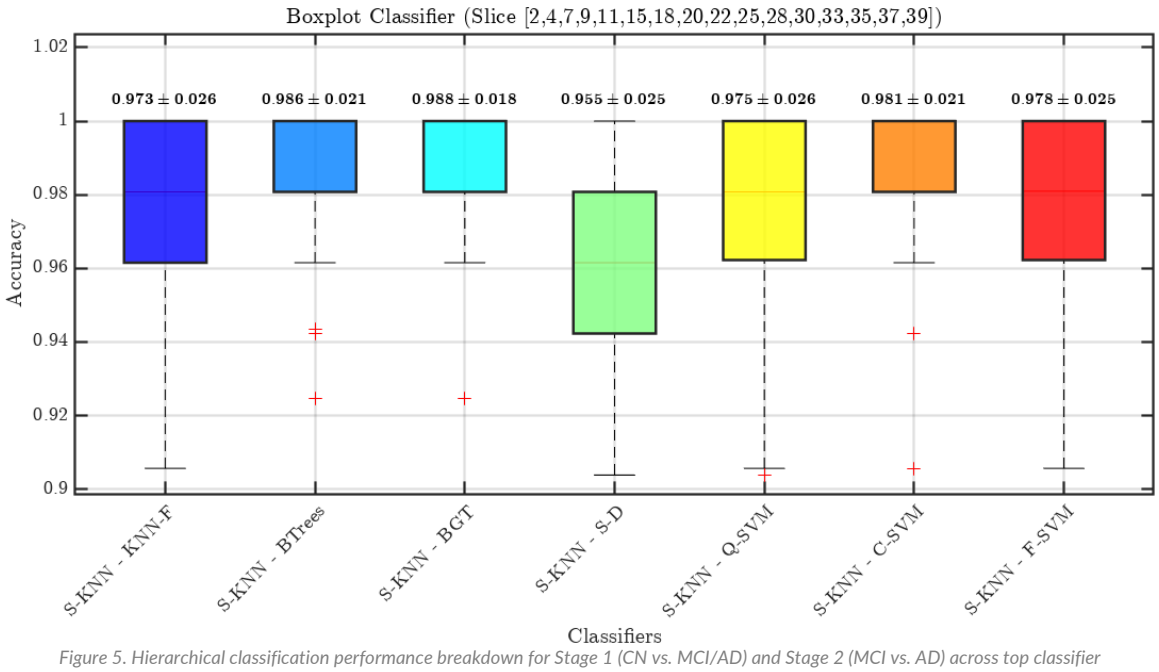


Figure 5. Hierarchical classification performance breakdown for Stage 1 (CN vs. MCI/AD) and Stage 2 (MCI vs. AD) across top classifier combinations.
Source: Own authorship

Analysis and Discussion

Early diagnosis of AD remains one of the most important clinical challenges, since the initial cognitive alterations are often subtle and difficult to detect using conventional diagnostic procedures. In this context, this study aimed to develop a methodology to identify patients in the early stages of AD by analyzing fMRI data. fMRI is a promising non-invasive biomarker because it can detect functional brain alterations associated with disease progression before severe clinical symptoms appear. Early identification of these alterations may facilitate the implementation of therapeutic and medical interventions aimed at delaying disease progression and improving patients' quality of life.

To address this challenge, we proposed a methodology based on relevant slice selection using ReliefF and spatial pattern characterization through the MCT. Initially, a qualitative inspection of the 49 available axial slices was performed, from which 40 slices containing visually relevant anatomical and functional information were selected. Next, we processed each slice independently using the MCT to enhance local spatial relationships among neighboring pixels. We then extracted statistical and shape descriptors to summarize each analysis window. Finally, we used the resulting feature vectors as input to the ReliefF algorithm, which ranked the slices by their discriminative power for differentiating the clinical states under study.

A. **Relevant Slice Selection:** After identifying the most representative slices through ReliefF, different experimental configurations were constructed using sets of $1, 2, 4, 8,$ and 16 slices. This strategy aimed to assess how additional spatial information from multiple brain regions affects classification performance. For each configuration, we evaluated both a multiclass classifier and a hierarchical classifier under identical experimental conditions, ensuring all classifiers received the same input information and enabling a fair comparison of their discriminative capabilities.
B. **Single-Slice Analysis:** As an initial baseline, the proposed methodology was evaluated using a single axial slice. The best-performing configuration corresponded to slice 36, where the hierarchical combination composed of a Fine KNN (KNN-F) classifier in the first stage and a Subspace KNN (S-KNN) classifier in the second stage achieved an accuracy of 0.915 ± 0.039. The class-wise accuracies were 0.928 ± 0.048 for $E1$, 0.895 ± 0.087 for $E2$, and 0.919 ± 0.066 for $E3$. For the same slice, the best multiclass result was obtained using a Fine KNN classifier, reaching an accuracy of 0.756. These findings indicate that even a single brain slice contains functional information relevant to Alzheimer's disease.
C. **Two-Slice Analysis:** Subsequently, combinations of two slices selected by ReliefF were evaluated. The best-performing combination corresponded to slices 8 and 24, achieving an accuracy of $0.961 \pm$

0.027 using the hierarchical classifier. For the same slice combination, the best multiclass result was approximately 0.776. In addition, the class-wise accuracies obtained by the hierarchical framework were 0.968 ± 0.038 for $E1$, 0.953 ± 0.051 for $E2$, and 0.960 ± 0.052 for $E3$.

D. **Four-Slice Analysis:** When the number of analyzed slices was increased to four, the best hierarchical configuration achieved an accuracy of 0.978 ± 0.023, whereas the best multiclass classifier obtained an accuracy close to 0.823. For this configuration, the classification accuracy of the clinically relevant E2 class reached 0.981 ± 0.038, demonstrating a substantial improvement compared with the single-slice and two-slice configurations.

E. **Eight-Slice Analysis:** The analysis of eight slices produced a considerable improvement in classification performance. The best hierarchical configuration achieved an accuracy of 0.993 ± 0.014, while the best multiclass classifier obtained an accuracy of approximately 0.893. The corresponding class-wise accuracies were 0.988 ± 0.024 for $E1$, 0.995 ± 0.026 for $E2$, and 1.000 ± 0.000 for $E3$.

F. **Sixteen-Slice Analysis:** The highest overall performance was obtained when 16 slices were analyzed simultaneously. In this scenario, the hierarchical classifier achieved a maximum accuracy of 0.994 ± 0.015, whereas the best multiclass classifier reached an accuracy of 0.895 for the same configuration. The best slice combination consisted of slices $6, 10, 13, 15, 17, 20, 22, 23, 26, 28, 30, 32, 35, 36, 37,39$, yielding class-wise accuracies of 0.993 ± 0.021 for $E1$, 0.997 ± 0.013 for $E2$, and 0.995 ± 0.024 for $E3$.

Another relevant finding was the predominance of nearest-neighbor-based classifiers among the best-performing configurations as shown in Figure 4 and Figure 5. In particular, the Subspace KNN (S-KNN) classifier appeared repeatedly within the highest-performing hierarchical models. In fact, the five best configurations obtained using 16 slices employed S-KNN in both stages of the hierarchical framework.

This behavior suggests that the feature spaces generated by the MCT naturally cluster samples belonging to the same class. Consequently, proximity-based methods are particularly effective at exploiting the intrinsic structure of the extracted features. In contrast, classifiers such as Fine KNN and several Support Vector Machine configurations appeared mainly in lower-performing solutions, especially when a limited number of slices were analyzed.

The results reveal a consistent trend: classification performance improves progressively as the number of slices analyzed increases. The overall accuracy of the hierarchical classifier increased from 0.915 ± 0.039 when a single slice was used to 0.994 ± 0.015 when 16 slices were analyzed. Similarly, the classification accuracy of E2 the class of greatest clinical interest increased from 0.895 ± 0.087 to 0.997 ± 0.013.

These findings indicate that the functional information associated with the early stages of AD is not concentrated in a single brain region but rather distributed across multiple regions. Therefore, incorporating additional slices provides complementary information that better represents disease-related functional patterns and improves the classification system's discriminative power.

Furthermore, the hierarchical classifier consistently outperformed the multiclass classifier across all evaluated configurations. While the best multiclass result achieved an accuracy of 0.895, the hierarchical framework reached 0.994 ± 0.015, representing an absolute improvement of approximately 10%. This behavior confirms that decomposing the original multiclass problem into two consecutive binary classification stages facilitates the discrimination of clinically similar states, particularly between $E2$ and $E3$.

Another important observation is the stability achieved during validation. The standard deviations for the best-performing configurations remained below 0.03, indicating high robustness across the data partitions generated through Monte Carlo validation. This suggests that the observed performance does not depend on a specific train-validation split and supports the proposed methodology's generalization capability.

The confusion matrices for both the multiclass and hierarchical schemes provide additional evidence of the proposed methodology's effectiveness. For the single-slice scenario (slice 36), the multiclass Fine KNN classifier exhibited considerable confusion between classes $E1$ and $E2$, correctly classifying only 52.0% of $E1$ samples. In comparison, 30.6% were incorrectly assigned to $E2$. In contrast, the hierarchical KNN-F/S-KNN configuration substantially improved the discrimination of E1, increasing its correct classification rate to 92.3% and reducing the confusion with $E2$ to 4.7%. Similar improvements were observed for $E2$ and $E3$, demonstrating the advantage of decomposing the problem into two consecutive binary decisions. When 16 slices were incorporated, the hierarchical S-KNN/S-KNN configuration achieved near-perfect discrimination, reaching classification rates of 98.9%, 98.7%, and 100% for $E1$, $E2$, and $E3$, respectively. These results indicate that integrating information from multiple ReliefF-selected slices significantly reduces class overlap

and enables more precise characterization of disease-related functional patterns, particularly for the clinically relevant early-stage $E2$.

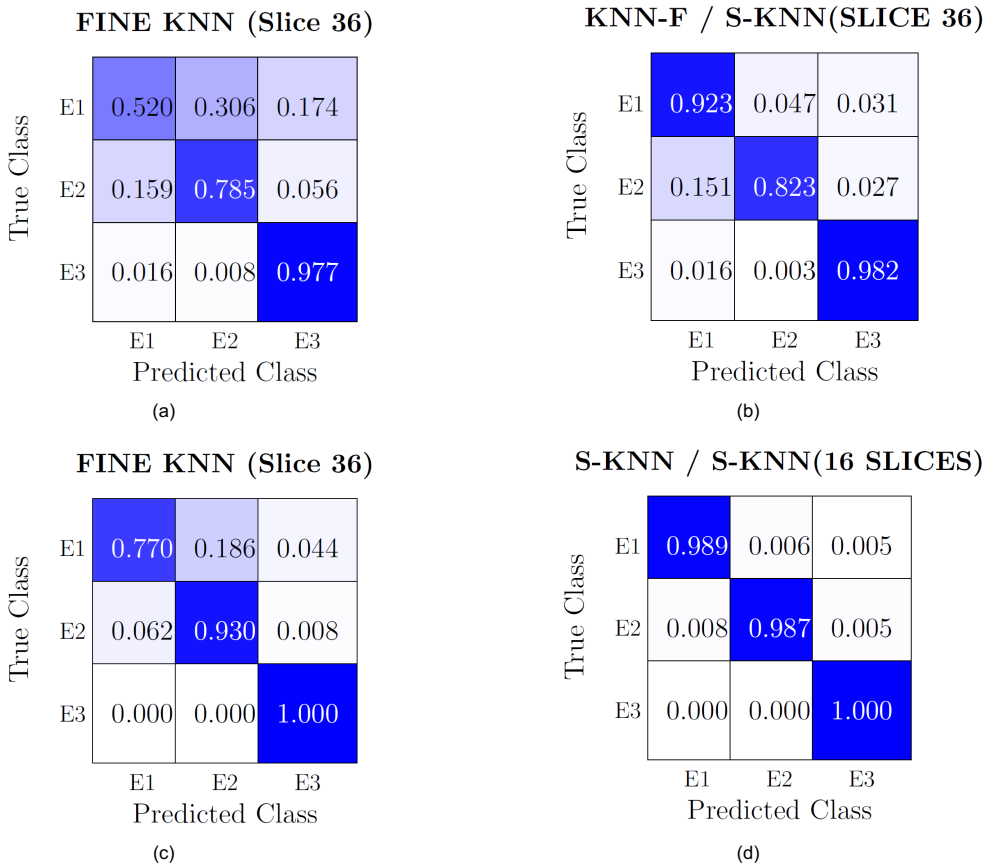


Figure 6. Confusion matrix and discriminative pattern analysis for axial slice 36 across clinical stages: (a) CN, (b) MCI, (c) AD, and (d) hierarchical stage comparison
Source: Own authorship

Overall, the results show that combining ReliefF-based slice selection, MCT-based feature extraction, and hierarchical classification provides a highly effective framework for early AD detection using fMRI data. The high accuracy achieved for the $E2$ class, the statistical stability observed throughout the experiments, and the consistent superiority of the hierarchical approach over the multiclass strategy support the proposed methodology as a computer-aided tool for early AD diagnosis. Moreover, the results suggest that a relatively small set of carefully selected slices contains sufficient information to characterize disease-related functional alterations without significantly compromising classification performance.

Furthermore, the proposed methodology achieved highly competitive results compared with recent studies reported in the literature. As shown in Table 2, Ahmad *et al*. (2023) obtained 98.70% accuracy using PCA and Artificial Neural Networks; Ullah *et al*. (2026) reported 99.15% with a lightweight CNN architecture; while multiclass studies by Mahapatra and Selvakumar (2025), Zolfaghari *et al*. (2025), Muksimova *et al*. (2025), Tan *et al*. (2026), and Ahmed (2025) achieved accuracies ranging from 94.20% to 99.04% using ensemble methods, deep learning models, attention mechanisms, and Vision Transformers.

In contrast, the proposed framework relies on MCT, a computationally efficient descriptor based on simple local neighborhood comparisons that capture disease-related spatial patterns without requiring complex feature-learning procedures. Despite its simplicity, the proposed hierarchical approach achieved an accuracy of 0.994 ± 0.015 and a classification accuracy of 0.997 ± 0.013 for the clinically relevant $E2$ stage. These results are comparable to, and in several cases surpass, those reported by more complex state-of-the-art approaches. Moreover, we evaluated all classifiers using the same input information and default MATLAB hyperparameters, without additional optimization. Consequently, the proposed methodology demonstrates that combining ReliefF-based slice selection, MCT feature extraction, and hierarchical classification can

provide high diagnostic performance while maintaining low computational cost, interpretability, and ease of implementation.

Table 2. *Performance comparison between the proposed methodology and state-of-the-art AD classification methods*

Work	Methodology	Stages of AD detected	Database	Classifier	Accuracy
Binary classification studies (CN vs. AD)					
Ahmad *et al*. (2023)	PCA feature extraction and Stepwise Linear Discriminant Analysis	CN vs. AD	ADNI	Artificial Neural Network (ANN)	98.70%
Mitra & Rehman (2024)	Kinematic, pressure, and temporal online handwriting feature extraction	CN vs. AD	DARWIN	Support Vector Machine (SVM)	92.86%
Ullah *et al*. (2026)	Lightweight architecture with depthwise separable convolutions and dense residual connections	Non-Demented vs. Demented	OASIS/ADNI	Lightweight CNN (LADNET)	99.15%
Multiclass classification studies (CN-MCI-AD / CN-EMCI-LMCI-AD)					
Mahapatra & Selvakumar (2025)	Nonlinear mathematical morphological modeling of ventricular dilation and SHAP explainability	CN vs. Very Mild vs. Mild Demented (3 classes)	OASIS-1	Random Forest / XGBoost	94.20%
Zolfaghari *et al*. (2025)	Dual parallel CN feature extraction with Search hyperparameter optimization	CN vs. Early MCI vs. Late MCI vs. AD (4 classes)	ADNI	Ensemble Learning (SVM + RF + KNN)	97.45%
Muksimova *et al*. (2025)	Multichannel CNN integrated with Convolutional Block Attention Module (CBAM)	CN vs. EMCI vs. LMCI vs. AD (4 classes)	ADNI	Attention-enhanced CNN	98.92%
Tan *et al*. (2026)	Compact CSF and structural MRI biomarker selection with univariate nonlinear activations	CN vs. MCI vs. AD (3 classes)	ADNI	Kolmogorov Arnold Networks (KANs)	97.35%
Ahmed (2025)	Pseudo-chromatic colormap transformation of single-channel MRI with path self-attention	CN vs. EMCI vs. LMCI vs. AD (4 classes)	ADNI	Vision Transformer (ViT)	99.04%
Ours	ReliefF (slice selection) + MCT	CN vs. MCI vs. AD (3 classes)	ADNI	Machine learning Hierarchical/ Multiclass	90.60% (1 slice) 99.40% (16 slices)

Source: Own authorship

Conclusions

The main objective of this study was to develop a methodology for early-stage AD identification by analyzing fMRI data using a non-invasive approach focused on detecting the $E2$ class, which represents the early stage of the disease. Early identification at this stage may enable timely therapeutic interventions to delay disease progression and improve quality of life. To address this challenge, we proposed a methodology that integrates ReliefF-based slice selection, feature extraction using the MCT, and statistical and shape descriptors. Since each fMRI study contains 49 axial slices, the proposed framework was designed to identify the most discriminative slices while reducing data dimensionality without compromising classification performance.

We investigated two classification strategies: a multiclass framework designed to discriminate among $E1$, $E2$, and $E3$ simultaneously, and a hierarchical framework composed of two consecutive binary classification stages. To evaluate the hierarchical approach thoroughly, we analyzed all 625 possible classifier combinations generated from the 25 classifiers available in MATLAB. Among these classifiers, Subspace KNN (S-KNN) consistently emerged as the predominant classifier in the highest-performing configurations, highlighting its suitability for the feature space generated by the proposed methodology.

The experimental results demonstrated that classification performance improved progressively as additional slices were incorporated into the analysis. Using a single slice, the hierarchical classifier achieved an accuracy of 0.915 ± 0.039, whereas the best configuration based on 16 slices reached 0.994 ± 0.015. Likewise, the classification accuracy of the clinically relevant E2 class increased from 0.895 ± 0.087 to 0.997 ± 0.013, confirming the proposed framework's ability to accurately identify patients in the early stages of Alzheimer's disease. Furthermore, the hierarchical strategy consistently outperformed the multiclass approach across all evaluated configurations, particularly when discriminating clinically similar states. Interestingly, the results obtained using 8 and 16 slices were very similar, suggesting that a relatively small number of carefully selected slices can provide sufficient information to achieve excellent classification performance while reducing computational complexity.

Finally, comparison with recently published studies shows that the proposed methodology achieves competitive results despite relying on a significantly simpler framework than many state-of-the-art deep learning approaches. The combination of ReliefF-based slice selection, MCT feature extraction, and hierarchical classification provides an efficient, interpretable, and computationally inexpensive solution for early AD detection using fMRI data. These findings support the proposed methodology as a practical computer-aided diagnostic tool and demonstrate that robust, accurate classification can be achieved without highly complex deep-learning architectures.

References

Abubakr, N., Kara, M., & Balık, H. H. (2026). Explainable Federated Attention-Based Deep Learning for Alzheimer's Disease Detection. *Applied Sciences.* https://doi.org/10.3390/app16104648

Ahmad, I., Siddiqi, M. H., Alhujaili, S. F., & Alrowaili, Z. A. (2023). Improving Alzheimer's Disease Classification in Brain MRI Images Using a Neural Network Model Enhanced with PCA and SWLDA. *Healthcare.* https://doi.org/10.3390/healthcare11182551

Ahmed, F. (2025). Colormap-Enhanced Vision Transformers for MRI-Based Multiclass (4-Class) Alzheimer's Disease Classification*. arXiv.* https://doi.org/10.48550/arXiv.2512.16964

Al-Otaibi, S., & Mujahid, M. (2024). Dual Attention Convolutional AutoEncoder for Diagnosis of Alzheimer's Disorder in Patients Using Neuroimaging and MRI Features. I*EEE Access*. https://doi.org/10.1109/ACCESS.2024.3390186

Al-bakri, F. H., Wan Bejuri, W. M. Y., Al-Andoli, M. N., Raja Ikram, R. R., Khor, H. M., Mispan, M. S., Yunos, N. M., Abd Yusof, N. F., Md Fauadi, M. H. F., & Jaya, A. S. M. (2025). A Hybrid Explainable AI Framework (HXAI) for Accurate and Interpretable Diagnosis of Alzheimer's Disease. *Diagnostics.* https://doi.org/10.3390/diagnostics15243118

Ali, S. S. A., Memon, K., Yahya, N., & Khan, S. (2025). Deep learning frameworks for MRI-based diagnosis of neurological disorders: a systematic review and meta-analysis. *Artificial Intelligence Review, 58(4),* 1-45. https://doi.org/10.1007/s10462-025-11146-5

Almalki, H., Khadidos, A. O., & Alhebaishi, N. (2024). Enhancing Alzheimer's detection: Leveraging ADNI data and large language models for high-accuracy diagnosis. *International Journal of Advanced Computer Science and Applications, 15(11),* 1134-1142. https://doi.org/10.14569/IJACSA.2024.01511134

Alorf, A. (2025). Transformer and Convolutional Neural Network: A Hybrid Model for Multimodal Data in Multiclass Classification of Alzheimer's Disease. *Mathematics, 13*(10), 1548 https://doi.org/10.3390/math13101548

Alsubaie, M. G. (2024). ConvADD: Exploring a Novel CNN Architecture for Alzheimer's Disease Detection. *International Journal of Advanced Computer Science and Applications*. https://doi.org/10.14569/IJACSA.2024.0150431

Arafa, D. A., Moustafa, H. E. D., Ali-Eldin, A. M. T., & Ali, H. A. (2022). Early detection of Alzheimer's disease based on the state-of-the-art deep learning approach: a comprehensive survey. *Multimedia Tools and Applications,* 81(25), 36471-36518. https://doi.org/10.1007/s11042-022-11925-0

Bayahya, A. Y., & Jammal, F. (2026). Hybrid deep learning and meta learning for Alzheimer disease classification via multimodal radiomic and visual features. S*cientific Reports.* https://doi.org/10.1038/s41598-026-64370-6

Chabib, C. M., & Hadjileontiadis, L. J. (2023). DeepCurvMRI: Deep Convolutional Curvelet Transform-Based MRI Approach for Early Detection of Alzheimer's Disease. I*EEE Access.* https://doi.org/10.1109/ACCESS.2023.3272482

Cilia, N. D., D'Alessandro, T., De Stefano, C., Fontanella, F., & Marcelli, A. (2021). From Online Handwriting to Synthetic Images for Alzheimer's Disease Detection Using a Deep Transfer Learning Approach. *IEEE Journal of Biomedical and Health Informatics*. 10.1109/JBHI.2021.3101982

Fröba, B., & Ernst, A. (2004). Face detection with the modified census transform. In Proceedings of the Sixth IEEE International Conference on Automatic Face and Gesture Recognition (pp. 91-96). *IEEE.* https://doi.org/10.1109/AFGR.2004.1301514

Ghahramani, H., Velaei, M., Piroozi, F., Ghaffari, A., & Yari, L. (2026). CortexNet: convolutional neural networks for alzheimer's disease diagnosis using brain MRI. Scientific Reports. https://doi.org/10.1038/s41598-026-63928-8

Govindarajan, P., Ananthu, M., Sarun, S., Kashyap, S., & Batumalay, M. (2026). NeuroCognex: multimodal brain signal analysis for Alzheimer disease prediction. *Discover Applied Sciences.* https://doi.org/10.1007/s42452-026-09323-4

Gupta, B., Jegannathan, G. K., Alam, M. S., Yogi, K. S., Ramesh, J. V. N., Sowmya, V. J., & Bayhan, I. (2025). Multimodal lightweight neural network for Alzheimer's disease diagnosis integrating neuroimaging and cognitive scores. *Neuroscience* Informatics. https://doi.org/10.1016/j.neuri.2025.100218

Hassan, N., Miah, A. S. M., Rahim, M. A., & Shin, J. (2025). Stacked CNN-based multichannel attention networks for Alzheimer disease detection. *Scientific Reports*. https://doi.org/10.1038/s41598-025-85703-x

Ibrar, W., Khan, M. A., Hamza, A., Rubab, S., Alqahtani, O., Turki-Hadj Alouane, M., Teng, S., & Nam, Y. (2025). A novel interpreted deep network for Alzheimer's disease prediction based on inverted self attention and vision transformer. *Scientific Reports.* https://doi.org/10.1038/s41598-025-15007-7

Kannan, S., Alzubi, J., Rajakumar, M., & Venugopal, S. (2026). Adaptive SE-attention ConvTransformer for Alzheimer's detection using MRI images. *EURASIP Journal on Advances in Signal Processing.* https://doi.org/10.1186/s13634-026-01344-w

Kung, C., Shaik, R., Javier, J., Dudhia, K., Bansal, V., & Kashyap, R. (2026). Artificial intelligence applied to neuroimaging in Alzheimer's disease: A scoping review of diagnostic, prognostic,

and biomarker-focused models. *Clinical Neuroimaging*, 2(1), e70014. https://doi.org/10.1002/neo2.70074

Lee, M., & Lee, S. (2026). Enhancing Early Alzheimer's Disease Detection via Transfer Learning: From Big Structural MRI Datasets to Ethnically Distinct Small Cohorts. *Applied Sciences.* https://doi.org/10.3390/app16021004

Leelavathi, R., Prabha Devi, D., Kodieswari, A., Khan, A. A., Suma, V., Kamal, S., & Ullah, F. (2026). A cloud enabled hybrid CNN transformer framework with attention mechanisms for scalable Alzheimer's disease staging from structural MRI. N*euroscience Informatics.* https://doi.org/10.1016/j.neuri.2026.100283

Lu, Y., Yu, H., Li, T., Meng, Y., & Lu, J. (2025). A lightweight CVTC model for accurate Alzheimer's MRI analysis and lesion annotation. *npj Digital Medicine.* https://doi.org/10.1038/s41746-025-02212-x

Mahapatra, K., & Selvakumar, R. (2025). Detection of Alzheimer's Disease using Explainable Machine Learning and Mathematical Models. *Journal of Medical Physics*. 10.4103/jmp.jmp_128_24

Mitra, U., & Rehman, S. U. (2024). ML-Powered Handwriting Analysis for Early Detection of Alzheimer's Disease. *IEEE Access.* https://doi.org/10.1109/ACCESS.2024.3401104

Muksimova, S., Umirzakova, S., Iskhakova, N., Khaitov, A., & Cho, Y. I. (2025). Advanced convolutional neural network with attention mechanism for Alzheimer's disease classification using MRI. C*omputers in Biology and Medicine.* https://doi.org/10.1016/j.compbiomed.2025.110095

Nawaz, K., Zanib, A., Wang, Y., Ayesha, N., Bahaj, S. A. O., & Mahmood, T. (2026). Optimized deep learning-based multistage Alzheimer's disease characterization with temporal modeling and soft-NMS for neuroimaging. *Discover Computing*. https://doi.org/10.1007/s10791-026-09938-6

Odusami, M., Maskeliūnas, R., & Damaševičius, R. (2023). Pixel-Level Fusion Approach with Vision Transformer for Early Detection of Alzheimer's Disease. *Electronics.* https://doi.org/10.3390/electronics12051218

Ogu, E. D., Nzelu, C. E., & John, S. N. (2024). The effects of machine learning algorithms in magnetic resonance imaging (MRI), and biomarkers on early detection of Alzheimer's disease. *Advances in Biomarker Sciences and Technology.* https://doi.org/10.1016/j.abst.2024.08.004.

Pandey, K. K., Mishra, A., & Milan, R. (2026). Predictive modeling approaches for Alzheimer's disease diagnosis through neuroimaging techniques: A comprehensive review. *Ageing Research Reviews,* 102989. https://doi.org/10.1016/j.arr.2025.102989

Rahman, S., Rahman, M. M., Bhatt, S., & Sundararajan, R. (2025). NeuroNet-AD: A Multimodal Deep Learning Framework for Multiclass Alzheimer's Disease Diagnosis. *Bioengineering*. https://doi.org/10.3390/bioengineering12101107

Rehman, S. U., & Mitra, U. (2025). Cognitive Handwriting Insights for Alzheimer's Diagnosis: A Hybrid Framework. *Information.* https://doi.org/10.3390/info16040249

Rehman, S. U., Tarek, N., Magdy, C., Kamel, M., Abdelhalim, M., Melek, A., Mahmoud, L. N., & Sadek, I. (2024). AI-based tool for early detection of Alzheimer's disease. *Heliyon*. https://doi.org/10.1016/j.heliyon.2024.e29375

Sharma, S., & Mandal, P. K. (2022). A comprehensive report on machine learning-based early detection of Alzheimer's disease using multi-modal neuroimaging data. *ACM Computing Surveys,* 55(2), 1-44. https://doi.org/10.1145/3492865

Sifat, M., Akter, S., Islam, A., Hamid, M. E., Miah, A. S. M., Hassan, N., Rahim, M. A., & Shin, J. (2026). 3D MRI-Based Alzheimer's Disease Classification Using Multi-Modal 3D CNN with

Leakage-Aware Subject-Level Evaluation. *arXiv*. https://doi.org/10.48550/arXiv.2603.17304

Tan, D., Song, L., Tang, Y., & Han, A. (2026). An interpretable multimodal framework using compact biomarkers and Kolmogorov–Arnold networks improves the early diagnosis of Alzheimer's disease. *Scientific Reports.* https://doi.org/10.1038/s41598-026-59430-w

Ullah, U., Habib, S., & Islam, M. (2026). LADNET: An MRI-based deep learning approach for Alzheimer's disease detection. *Computers in Biology and Medicine*. https://doi.org/10.1016/j.compbiomed.2026.111647

Vrahatis, A. G., Skolariki, K., Krokidis, M. G., Lazaros, K., Exarchos, T. P., & Vlamos, P. (2023). Revolutionizing the early detection of Alzheimer's disease through non-invasive biomarkers: The role of artificial intelligence and deep learning. *Sensors,* 23(9), 4184. https://doi.org/10.3390/s23094184

Wang, Y., Sheng, H., & Wang, X. (2025). Recognition and diagnosis of Alzheimer's Disease using T1-weighted magnetic resonance imaging via integrating CNN and Swin vision transformer. *Clinics*. https://doi.org/10.1016/j.clinsp.2024.100673

Wang, Y., Wang, Q., Zhou, M., Liang, J., You, L., Asken, B., Zhou, X., & Song, Q. (2025). Integration of Genetic and Imaging Data for Alzheimer's Disease Diagnosis and Interpretation. Advanced Science. https://doi.org/10.1002/advs.202409549

Yu, Q., Ma, Q., Da, L., Li, J., Wang, M., Xu, A., Li, Z., & Li, W. (2024). A transformer-based unified multimodal framework for Alzheimer's disease assessment. Computers in Biology and Medicine. https://doi.org/10.1016/j.compbiomed.2024.108979.

Almansour, A. G. M., Alshomrani, F., Almutairi, A. T. M., Alalwany, E., Alshuhri, M. S., Alshaari, H., & Alfahaid, A. (2025). DA-ViT: Deformable Attention Vision Transformer for Alzheimer's Disease Classification from Structural MRI. *Computer Modeling in Engineering & Sciences.* https://doi.org/10.32604/cmes.2025.069661

Zolfaghari, S., Joudaki, A., & Sarbaz, Y. (2025). A hybrid learning approach for MRI-based detection of alzheimer's disease stages using dual CNNs and ensemble classifier. Scientific Reports. https://doi.org/10.1038/s41598-025-11743-y

Zubair, M., Jaffar, A., Hussain, S., & Akram, S. (2025). Alzheimer's disease classification using a hybrid deep learning approach with multi-layer U-net segmentation and XAI driven analysis. PLOS ONE. https://doi.org/10.1371/journal.pone.0332572